

Phenomenology of Avalanche Recordings from Distributed Acoustic Sensing

Patrick Paitz¹, Nadja Lindner², Pascal Edme², Pierre Huguenin³, Michael Hohl⁴, Betty Sovilla⁴, Fabian Walter³, and Andreas Fichtner²

¹Swiss Federal Institute for Forest Snow and Landscape Research (WSL)

²ETH Zürich

³Swiss Federal Institute for Forest Snow and Landscape Research (WSL)

⁴WSL Swiss Federal Institute for Snow and Avalanche Research (SLF)

December 7, 2022

Abstract

Avalanches and other hazardous mass movements pose a danger to the population and critical infrastructure in alpine areas. Hence, understanding and continuously monitoring mass movements is crucial to mitigate their risk. We propose to use Distributed Acoustic Sensing (DAS) to measure strain rate along a fiber-optic cable to characterize ground deformation induced by avalanches. We recorded 12 snow avalanches of various dimensions at the Vallée de la Sionne test site in Switzerland, utilizing existing fiber-optic infrastructure and a DAS interrogation unit during the winter 2020/2021. By training a Bayesian Gaussian Mixture Model, we automatically characterize and classify avalanche-induced ground deformations using physical properties extracted from the frequency-wavenumber and frequency-velocity domain of the DAS recordings. The resulting model can estimate the probability of avalanches in the DAS data and is able to differentiate between the avalanche-generated seismic near-field, the seismo-acoustic far-field and the mass movement propagating on top of the fiber. By analyzing the mass-movement propagation signals, we are able to identify group velocity packages within an avalanche that propagate faster than the phase velocity of the avalanche front, indicating complex internal structures. Importantly, we show that the seismo-acoustic far-field can be detected before the avalanche reaches the fiber-optic array, highlighting DAS as a potential research and early warning tool for hazardous mass movements.

1 **Phenomenology of Avalanche Recordings from**
2 **Distributed Acoustic Sensing**

3 **Patrick Paitz¹, Nadja Lindner², Pascal Edme², Pierre Huguenin³, Michael**
4 **Hohl³, Betty Sovilla³, Fabian Walter¹, Andreas Fichtner²**

5 ¹WSL, Swiss Federal Institute for Forest, Snow and Landscape Research, Birmensdorf, Switzerland

6 ²ETH Zurich, Department of Earth Sciences, Institute of Geophysics, Seismology and Wave Physics

7 ³SLF, WSL Institute for Snow and Avalanche Research SLF, Davos, Switzerland

8 **Key Points:**

- 9 • DAS measurements near the interface between avalanche and the subsurface re-
10 veal flow dynamics.
- 11 • Strain rate measurements of seismo-acoustic waves are registered up to 30 s be-
12 fore avalanches reach the sensors.
- 13 • Internal group velocities larger than the propagation speed suggest the presence
14 of complex internal structures.

Abstract

Avalanches and other hazardous mass movements pose a danger to the population and critical infrastructure in alpine areas. Hence, understanding and continuously monitoring mass movements is crucial to mitigate their risk. We propose to use Distributed Acoustic Sensing (DAS) to measure strain rate along a fiber-optic cable to characterize ground deformation induced by avalanches. We recorded 12 snow avalanches of various dimensions at the Vallée de la Sionne test site in Switzerland, utilizing existing fiber-optic infrastructure and a DAS interrogation unit during the winter 2020/2021. By training a Bayesian Gaussian Mixture Model, we automatically characterize and classify avalanche-induced ground deformations using physical properties extracted from the frequency-wavenumber and frequency-velocity domain of the DAS recordings. The resulting model can estimate the probability of avalanches in the DAS data and is able to differentiate between the avalanche-generated seismic near-field, the seismo-acoustic far-field and the mass movement propagating on top of the fiber. By analyzing the mass-movement propagation signals, we are able to identify group velocity packages within an avalanche that propagate faster than the phase velocity of the avalanche front, indicating complex internal structures. Importantly, we show that the seismo-acoustic far-field can be detected before the avalanche reaches the fiber-optic array, highlighting DAS as a potential research and early warning tool for hazardous mass movements.

Plain Language Summary

Avalanches and other hazardous mass movements pose a danger to the population and critical infrastructure in alpine areas. Therefore it is important to be able to reliably measure and detect these hazardous events. We show a successful example to measure and characterize avalanches recorded with a Distributed Acoustic Sensing (DAS) device, that measures deformation along a fiber optic cable. We apply unsupervised machine learning to our avalanche recordings, and are able to identify consistent properties between 12 avalanches. Ultimately, our results indicate that DAS might be a useful tool for detecting hazardous mass movements.

1 Introduction

1.1 Motivation

Practically all mountainous regions worldwide are subject to some forms of rock falls, snow/rock/ice avalanches, debris flows and sediment-transporting floods. These rapid mass movements pose a significant hazard to both the population and infrastructure, with billions of dollars in financial damage and thousands of fatalities each year (Emberson et al., 2020; Dille, 2005; Froude & Petley, 2018; Petley, 2012). According to the 2021 Intergovernmental Panel on Climate Change (IPCC) report, the *"magnitude of debris flows might increase [...] and the debris-flow season may last longer in a warmer climate"* (Zhongming et al., 2021). This suggests that global warming will exacerbate the hazard potential of debris flows and various types of related mass movements. To early detect destructive events and mitigate their impact, extensive, reliable and high resolution monitoring and warning solutions are crucial. Seismic and acoustic instruments are increasingly popular for mass movement monitoring, since they record signatures of hazardous events even kilometers away from their occurrence without the need for a direct line of sight between source and sensor (Allstadt et al., 2018; Marchetti et al., 2019). The combination of unrivaled temporal resolution of seismic records and wide spatial sensitivity is a pivotal advantage over in situ measurements (Arattano & Marchi, 2008) and remote sensing approaches like radar technology (Leinss et al., 2020).

62 Implementation of seismic measurements into operational mass movement warn-
 63 ing has to fulfill two requirements. First, the seismic sensors have to be placed in var-
 64 ious locations to maximize coverage of failure-prone terrain. Second, the detection al-
 65 gorithms have to handle real-time data streams and reliably recognize significant tell-
 66 tale signals in the presence of environmental and anthropogenic noise.

67 Seismic instrumentation has in recent years undergone rapid developments towards
 68 more portable sensors (Leinss et al., 2020). However, even in densely instrumented coun-
 69 tries like Switzerland, sensor coverage is still insufficient to encompass significant amounts
 70 of unstable slopes. In view of snow avalanches, in particular, the typically harsh terrain
 71 in avalanche-prone regions tends to limit the spatial coverage and temporal resolution
 72 of most measurements, and of seismic arrays in particular (Pérez- Guillén et al., 2016).
 73 Furthermore, recent improvements in machine learning algorithms show great promise
 74 for the automatic recognition of emergent and complicated mass movements seismograms
 75 (Chmiel et al., 2021). Yet further improvements are necessary to recognize events at sites
 76 where little or no training data are available and to identify signal characteristics, which
 77 reveal scientific insights into the dynamic characteristics of mass movements.

78 Here we address these open challenges with the applications of Distributed Acoustic
 79 Sensing (DAS) for snow avalanche detection and characterization. DAS is a technique
 80 to measure strain or strain rate along a fiber-optic cable with sub-meter resolution and
 81 mHz to kHz frequency bandwidth (Lindsey et al., 2020; Paitz et al., 2021). Unused fiber-
 82 optic infrastructure initially installed for communication purposes can thus be turned
 83 into countless seismic sensors increasing spatial coverage of seismic measurements. We
 84 leverage the dense seismic sensing of DAS with unsupervised algorithms to automati-
 85 cally recognize snow avalanches and their internal properties, offering new perspectives
 86 for monitoring and alarm systems.

87 1.2 Fiber-Optic Sensing in a Natural Hazard Context

88 The introduction of distributed fiber-optic sensing systems to geophysics marks a
 89 milestone. By turning a fiber-optic cable into a high resolution seismic measurement net-
 90 work, fiber-optic sensing technologies have opened up new possibilities in exploration geo-
 91 physics and passive seismology (Lindsey & Martin, 2021; Zhan, 2019), especially in dif-
 92 ficult terrain like glaciers and volcanoes (Klaasen et al., 2021; Walter et al., 2020) or on
 93 the bottom of the ocean (Lindsey et al., 2019; Williams et al., 2019). For more background
 94 information on fiber-optic sensing, the reader is referred to Hartog (2017).

95 In the context of natural hazards, Brillouin-based distributed fiber-optic sensing
 96 systems (BOTDA) have been utilized for landslide and deformation monitoring (Iten et
 97 al., 2008; Minardo et al., 2018), and coherent optical time-domain reflectometry (COTDR)
 98 was successfully used for ground motion and deformation measurements on landslides
 99 (Yu et al., 2018). The suitability of optical time-domain reflectometry (OTDR) systems
 100 like the Silixa iDAS(TM) Distributed Acoustic Sensing unit (used in this study) for the
 101 recording of acoustic emission precursors in soil in a laboratory setting was also already
 102 established several years ago (Michlmayr et al., 2017). The study by Walter et al. (2020)
 103 used a similar DAS system to successfully monitor rockfalls and icequakes on a glacier.
 104 Early studies by Prokop et al. (2014) explored avalanche monitoring with fiber-optic sens-
 105 ing systems for avalanche detection and runout distance monitoring.

106 2 Experiment Setup and Recorded Avalanches

107 We utilized a Silixa iDAS(TM) v2.4 interrogation unit on an existing fiber-optic
 108 cable at the Vallée de la Sionne avalanche test site in Switzerland from October 2020 to
 109 March 2021. A map and a photograph of the test-site are shown in Fig. 1. The test site
 110 has been operated by the WSL Institute for Snow and Avalanche Research SLF for over
 111 20 years (Ammann, 1999). Several sensor points within the avalanche paths and runout

112 zones feature seismic, pressure and radar sensors and are connected via fiber-optic ca-
 113 bles to a bunker at the valley bottom where data are stored and processed. The length
 114 of the interrogated fiber was around 800 m, and the interrogator was located in the bunker,
 115 positioned at the bottom of the path. The fiber crosses the La Sionne creek around 700
 116 m from the topmost monitoring point. Over the entire array, the (single-mode) fiber is
 117 installed in a conduit that was excavated to a depth of less than a meter during the con-
 118 struction of the test site. This protects the fiber against avalanche damages. The sam-
 119 pling rate of the interrogator was 1 kHz at a spatial sampling of 2 m.

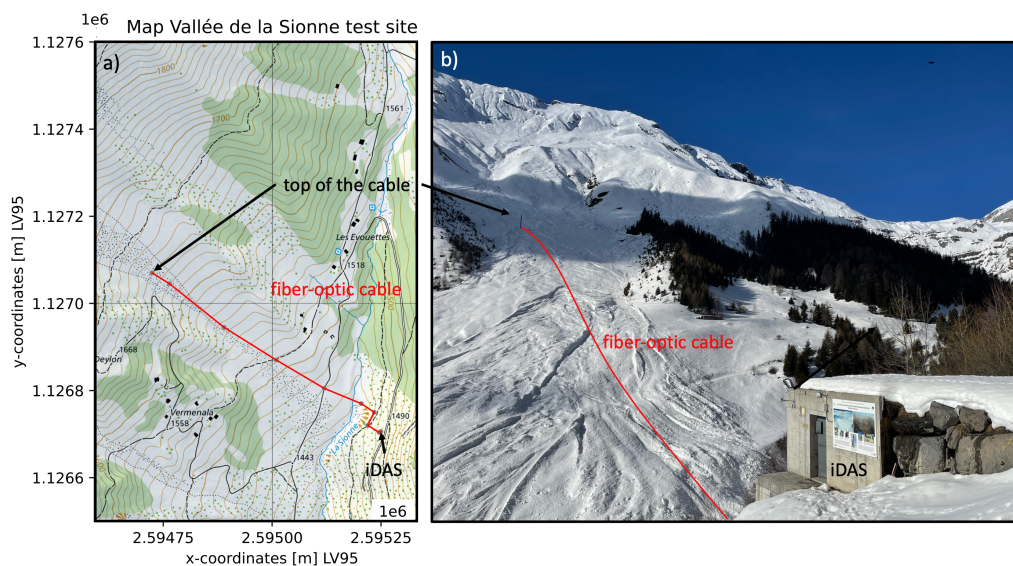


Figure 1. Test site overview. **a)** Map view of the Vallée de la Sionne avalanche test site. Map from SwissTopo (2021). **b)** Photograph of the test-site area with the approximate fiber position indicated in red. The DAS interrogation unit was located in the bunker (building in the lower right corner).

120 During the data acquisition period, more than 20 DAS recordings of avalanches were
 121 registered. In this manuscript, we first discuss the key characteristics for one example
 122 (denoted "avalanche 3023"). This one was selected since it contains key features while
 123 still being not too complex. For 12 additional events, the data are visualized in the sup-
 124plementary material. The recorded data of the observed avalanches cover large transi-
 125tional powder snow avalanches with partial flow regime transitions and depositional regimes
 126(avalanches 3009, 3022 and 3023) and smaller avalanches without a clearly distinguish-
 127able transition (avalanches 3016, 3020 and 3021). A summary of the measured avalanches
 128is given in Tab. B1 in the appendix.

129 3 Avalanche Recordings: Phenomenology

130 All avalanches considered in this study propagated on top of the fiber-optic cable.
 131 Therefore, the data contain a superposition of near-field observations of seismo-acoustic
 132 sources, as well as ground vibrations from sources that can potentially be further away.
 133 Note that we prefer the term "seismo-acoustic" over "seismic" as seismic records of avalanches
 134 may contain signatures of waves traveling through the air (Heck, Hobiger, et al., 2019).
 135 For particulate gravity currents like snow avalanches, various theoretical models for seis-
 136mogenesis have been recently proposed, which form the basis for the following discus-

137 sion. Nevertheless, air waves such as infrasound may also contain important informa-
 138 tion about avalanche volumes and dynamics and could influence our DAS records (Allstadt
 139 et al., 2018; Marchetti et al., 2021).

140 For multiphase flows (granular flow in dense flow regimes and turbulent flow in the
 141 aerial components) such as snow avalanches, different seismic source mechanisms have
 142 been considered in the past: (1) (quasi-)static deformation as a response to instantaneous
 143 weight and frictional shear forces (Wenner et al., 2022) and (2) (snow) particle-ground
 144 impacts (Tsai et al., 2012), (3) turbulent flow (Gimbert et al., 2014) and, by (4) abrupt
 145 stopping of mass movement due to friction (Tregaskis et al., 2022), and by (5) changes
 146 in traction due to mass deposition and erosion (Edwards & Gray, 2015). A schematic
 147 avalanche propagating over our fiber array is shown in Fig. A1 in the appendix.

148 **3.1 DAS data**

149 **3.1.1 Time-Distance Domain**

150 The raw data of avalanche 3023 are visualized in Fig. 2. The total duration of the
 151 avalanche propagating over the array is about two minutes. The ground truth of the avalanche
 152 is confirmed by measurements of the GEODAR system (Keylock et al., 2014; Köhler,
 153 McElwaine, & Sovilla, 2018). The extent of the avalanche as measured by the GEODAR
 154 is highlighted in transparent blue colors in Fig. 2. Different parts of the avalanche can
 155 be distinguished (where the numbers correspond to the features highlighted in the fig-
 156 ure): (1) The earlier, faster part of the avalanche between 0.5 and 1.0 minutes time, and
 157 (2) a slower, later part of the avalanche between 1.0 and 2.5 minutes. What is also vis-
 158 ible is that (5) there are signals arriving over the entire array before the avalanche front
 159 moves on top of the cable (at times before 0.75 minutes). Other observable features in-
 160 clude (4) noisier channels (e.g. at 310 meters), and (3) high amplitude and velocity events
 161 (nearly horizontal in the plot), spanning about 100 m in distance each. These events could
 162 be interpreted as (abrupt) stopping events, where parts of the avalanche abruptly de-
 163 celerate, hence creating a high amplitude strain-change in the subsurface. Other poten-
 164 tial explanations for these events include snowpack collapses. However the fact that the
 165 strain-rate amplitudes of the mass-movement is significantly lower after these events makes
 166 the abrupt stop hypothesis more likely. It must be noted that for distances above 200
 167 m along the fiber, there is no clear DAS signal visible in the raw and low-frequency data,
 168 whereas the GEODAR outline still records an avalanche signal there. The low-frequency
 169 time-offset strain rate data are also visualized in Panel b) of Fig. 2. The two main parts
 170 of the avalanche (1) and (2), as well as the stopping mechanisms (3) are still visible, and
 171 the data look less noisy compared to the raw data in Fig. 2a).

172 **3.1.2 Frequency-Wavenumber Domain**

173 Since the fiber is approximately straight with equal channel spacing over the en-
 174 tire array, it is straightforward to analyze the data in the frequency-wavenumber domain.
 175 The frequency-wavenumber representation of the data is defined as a 2-D Fourier Trans-
 176 form (over time and over space):

$$\dot{\epsilon}(f, k) = \int_x \int_t \dot{\epsilon}(t, x) e^{-2\pi i f t} e^{-2\pi i k x} dt dx, \quad (1)$$

177
 178 for the strain rate $\dot{\epsilon}$, time t , distance x , frequency f and wavenumber k (the inverse
 179 of the wavelength). This representation allows for analysis of the frequency and appar-
 180 ent phase velocity content of the data and can reveal dispersive behavior, i.e. frequency
 181 dependence of the velocity of individual wave modes.

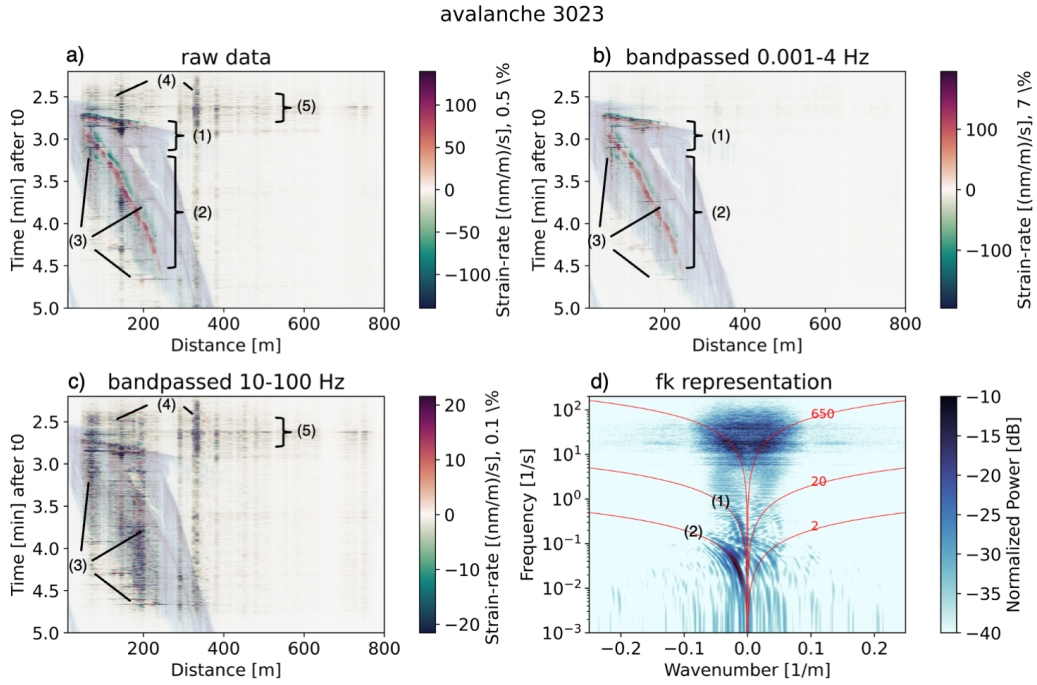


Figure 2. **a)** Raw strain rate data of avalanche 3023. The amplitudes are clipped at 0.5% of the global maximum within the visualized window. **b)** Bandpass filtered low-frequency strain rate data of avalanche 3023 (4th order Butterworth bandpass filter from 0.001 to 10 Hz). The amplitudes are clipped at 7 % of the global maximum within the visualized window. **c)** Bandpassed high-frequency strain rate data of avalanche 3023 (4th-order Butterworth bandpass filter from 10 to 100 Hz). The amplitudes are clipped at 0.1 % of the global maximum within the visualized window. For a) to c), the ground truth of the extent of the avalanche is highlighted in transparent blue from the measurements of the GEODAR system. **d)** Frequency-wavenumber (fk) representation of the raw data from avalanche 3023. The red lines indicate apparent phase velocities along the array in m/s. Negative wavenumbers indicate energy propagating from the top to the bottom of the slope (downward), and positive wavenumbers indicate coherent energy propagating upward. The distance starts at the Northwest end of the cable (uphill) at 0 m and ranges down to the Southeast end of the cable in the bunker, where the interrogator was located (Fig. 1).

182 The frequency-wavenumber (fk) representation of the raw data of avalanche 3023
 183 is visualized in Fig. 2d. From the fk representation of the data, a clear separation can
 184 be observed between high-frequency seismic (10 - 30 Hz) and low-frequency (0.01 to 10
 185 Hz) signals. The two different parts of the avalanche observed in the raw data are also
 186 visible in the fk domain (features (1) and (2)) for frequencies below 1 Hz. The fk vi-
 187 sualization associates these low-frequency (< 1 Hz) downward propagating signals with
 188 phase velocities of between 5 to 20 m/s (1), and 2 m/s (2). In addition, high-velocity events
 189 are visible for frequencies between 5 and 30 Hz, propagating both up- and downward at
 190 speeds of about 650 m/s. Such apparent velocities and the omnidirectional propagation
 191 suggest that these events are seismic waves generated by the avalanche.

192 4 Signal classification

193 In order to automatically identify and distinguish between the signals shown in Fig.
 194 2, we propose the use of unsupervised machine learning algorithms. In the past, unsu-
 195 pervised algorithms have proven useful in a geophysical context to extract subsets of sig-
 196 nals with similar properties from large datasets (Martin et al., 2018; Grimm, 2021; Grimm
 197 & Poli, 2022). In a cryoseismic context, Grimm (2021) extracted different physical classes
 198 from continuous DAS recordings on a glacier, characterizing crevassing events, stick-slip
 199 icequakes and background noise in an automated way. Similarly, Grimm and Poli (2022)
 200 used spatial coherency features of an urban DAS dataset from Grenoble (France) to iden-
 201 tify spatio-temporally repeating events. Martin et al. (2018) utilized signal features from
 202 data segments that had been transformed using the continuous wavelet transform and
 203 minibatch-optimized K-means to find classes of coherent properties of the seismic wave-
 204 field from DAS data. Here we propose to use unsupervised clustering to identify char-
 205 acteristic properties of avalanche recordings with DAS. Since the dimensionality of the
 206 DAS data is too high to perform clustering on raw data, we first extract representative
 207 features. This is a common first step in applied machine learning workflows, and the cho-
 208 sen features have to be chosen problem-dependent (Alpaydin, 2020).

209 4.1 Feature Extraction

210 Automatic and (near) real-time processing for warning applications requires sig-
 211 nal feature extraction within small time- and space windows. These windows contain ei-
 212 ther avalanche signals and/or background noise, which includes natural (e.g., earthquake)
 213 and anthropogenic (e.g., road and air traffic) signals. We set the window sizes to 5 s in
 214 time and 50 m in space (with adjacent windows overlapping by 3 s and 30 m). The win-
 215 dow size and overlap was chosen empirically such that coherent signals in time and space
 216 are detected, while small-scale changes are still captured.

217 Our proposed feature extraction algorithm is visualized in Fig. 3. In the first step,
 218 the raw data are windowed and transformed to the fk domain (see Eq. 3.1.2). In the
 219 fk domain, the contents of the amplitude spectrum of velocity-frequency bins are an-
 220 alyzed, resulting in cumulative fk amplitudes \dot{A} for each bin, where the dot indicates
 221 that the cumulative fk amplitudes are associated with a transformation of strain rate
 222 $\dot{\epsilon}$ rather than strain.

$$\dot{A}(v_1, v_2, f_1, f_2) = \sum_{f,k} |\dot{\epsilon}(f, k)|; \quad \forall v = \frac{f}{k} \in \{v_1, v_2\} \cap f \in \{f_1, f_2\}, \quad (2)$$

223 where the local phase velocity v can be described in terms of frequency f and wavenum-
 224 ber k , following $v = f/k$. The frequency and velocity bins range from f_1 to f_2 and from
 225 v_1 to v_2 , respectively. The above equation maps our data from the fk domain into a dis-
 226 crete velocity-frequency (vf) domain. In the next step, we find n numbers of local max-
 227 ima in this domain and extract the corresponding frequency and apparent velocity of these
 228 maxima, for both positive and negative wavenumbers. This results in n local maxima

229 for positive wavenumbers and negative wavenumbers:

$$M_n^+(v_{n^+}, f_{n^+}) = \max(\dot{A}(v, f)); \forall n^+ \in \{1 \dots n\} \cap k > 0 \quad (3)$$

$$M_n^-(v_{n^-}, f_{n^-}) = \max(\dot{A}(v, f)); \forall n^- \in \{1 \dots n\} \cap k < 0 \quad (4)$$

230 For each of these peaks $M_n(v_n, f_n)$, we compute the ratio $R(v_n, f_n)$ between the
 231 cumulative fk amplitudes \dot{A} of positive and negative wavenumber, giving us an indica-
 232 tion of a preferable directionality in propagation:

$$R_n^+(v_{n^+}, f_{n^+}) = \frac{\dot{A}(v_{n^+}, f_{n^+})}{\dot{A}(-v_{n^+}, f_{n^+})}; \forall n^+ \in \{1 \dots n\} \cap k > 0 \quad (5)$$

233

$$R_n^-(v_{n^-}, f_{n^-}) = \frac{\dot{A}(-v_{n^-}, f_{n^-})}{\dot{A}(v_{n^-}, f_{n^-})}; \forall n^- \in \{1 \dots n\} \cap k < 0 \quad (6)$$

234 In addition to the values of the peaks $M_n^{+-}(v_n, f_n)$ in the vf domain, we extract
 235 information on the summed amplitude spectrum S , defined as:

$$S^+ = \sum_{f,k} |\dot{\epsilon}(f, k)|; \forall k > 0 \quad (7)$$

236

$$S^- = \sum_{f,k} |\dot{\epsilon}(f, k)|; \forall k < 0 \quad (8)$$

237 The last feature we extract is the ratio of cumulative amplitudes between positive and
 238 negative wavenumbers C within the specific time-space window:

$$C = \frac{S^+}{S^-}. \quad (9)$$

239 For each window, a total of 11 features are extracted per picked peak n as summarized
 240 in Tab. 1. This reduces the dimensionality for each window from 62500 (2500 samples
 241 for 25 channels) to $11 \cdot n$, which is $< 0.1\%$ of the dimensionality of the raw data. In our
 242 case, n was chosen to be 3 in order to capture first, second and third order effects within
 243 each window. The features encode the apparent phase velocities, frequency content, dom-
 244 inant propagation direction and total strain rate energy within each window, and hence
 245 describe physical properties that are potentially important for avalanche characteriza-
 246 tion and discrimination from other signals like earthquakes.

247 4.2 Bayesian Gaussian mixture models: Unsupervised Clustering

248 The features in Tab. 1 are used in an unsupervised clustering algorithm to identi-
 249 fy groups of data with similar properties. We chose a Bayesian Gaussian mixture model
 250 after evaluating the performance of various clustering algorithms including K-means, mini-
 251 batch K-means, and affinity propagation (Bishop & Nasrabadi, 2006; Press et al., 2007).

252 Bayesian Gaussian mixture models are probabilistic models that fit training data
 253 onto a finite number of Gaussian distributions, utilizing the Expectation-Maximization
 254 algorithm (see Bishop and Nasrabadi (2006); Press et al. (2007) for details). This way,
 255 each feature-set of the training data is associated to a cluster, or class (one of the Gaus-
 256 sian distributions). Compared to other conventional clustering algorithms like K-Means,
 257 Gaussian mixture models have the advantage that a trained model can predict a class
 258 from data that it was not trained with. Furthermore, instead of associating one class to
 259 a set of features (hard assignment of data points to a cluster), the probability of the data
 260 for being a part of each subclass is estimated (soft assignment of data points to a class
 261 from the posterior probabilities for each class) (Bishop & Nasrabadi, 2006), which in our

Table 1. Features extracted in each sub-window of the DAS record that are used for the characterization of the data.

Feature	Description
$M^+(v_{n+}, f_{n+})$	local maxima in the vf domain for positive k
$M^-(v_{n-}, f_{n-})$	local maxima in the vf domain for negative k
v_{n+}, v_{n-}	apparent phase velocity of the local maximum M for pos. (+) and neg. (-) k
f_{n+}, f_{n-}	frequency of the local maximum M for pos. (+) and neg. (-) k
$R^+(v_{n+}, f_{n+})$	ratio between $M^+(v_{n+}, f_{n+})$ and corresponding vf amplitudes of neg. k
$R^-(v_{n-}, f_{n-})$	ratio between $M^-(v_{n-}, f_{n-})$ and corresponding vf amplitudes of pos. k
S^+	cumulative amplitude spectrum in the fk domain for positive k
S^-	cumulative amplitude spectrum in the fk domain for negative k
C	ratio between S^+ and S^-

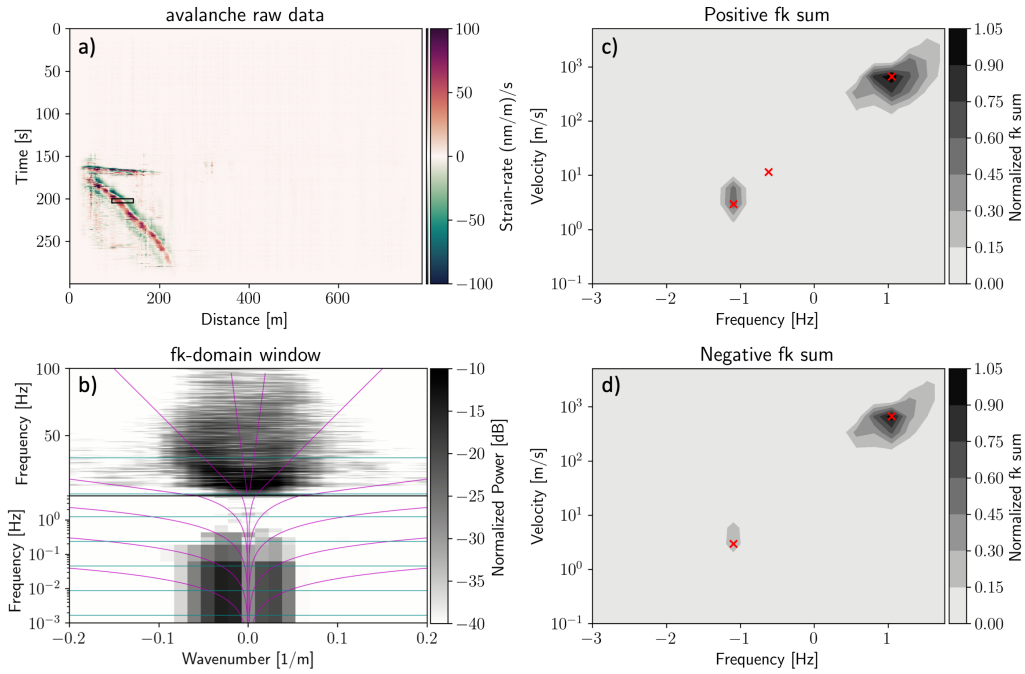


Figure 3. Example of the windowed algorithm proposed to extract signal properties used to detect and characterize avalanche data. **a)** In a first step, the data are windowed in both time and space (indicated by the black rectangle). In our example, the length of the window is 50 m and 5 s. **b)** The windowed data are then tapered (in both time and space) and transformed to the fk domain. The fk domain is then binned into frequency ranges (indicated by the horizontal blue lines) and velocity ranges (indicated by the magenta diagonal curves). For each bin, the absolute values of the fk amplitudes are then summed and normalized over the number of samples per bin. The fk domain amplitudes are displayed in dB relative to the maximum fk amplitudes. **c)** and **d)** The output of the bottom left is then arranged by frequency and velocity, and local maxima are extracted. This results in a number of n (in this example $n = 3$) extracted peaks, with corresponding frequency and velocity ranges, as well as summed fk amplitude values. The process is done for positive wavenumber values and for negative wavenumber values. For each peak, the ratio of positive to negative fk amplitude is also stored as a feature.

262 case becomes important where low-frequency low-velocity mass movements are within
 263 the same space time window as high-frequency seismic waves. We use the python pack-
 264 age scikit-learn (Pedregosa et al., 2011) for the implementation of Bayesian Gaussian mix-
 265 ture models. Based on trial and error, we decided to set the number of classes to 10, ini-
 266 tializing the weights, means and covariances with the K-means algorithm, and using a
 267 Dirichlet process for the weight concentration prior. Increasing the number of classes re-
 268 sulted in a higher number of "noise" classes without improving the signal classification.
 269 Decreasing the number of classes led to inconsistent clustering results for multiple stages
 270 of training.

271 We train the model with 92367 windows from 13 potential avalanche candidates,
 272 including windows containing environmental and anthropogenic noise, avalanches, and
 273 earthquake recordings. In total, 246118 feature sets are used as input for the training
 274 (where for some of the windows, less than 3 feature sets could be extracted). After train-
 275 ing, the model can be used to estimate the probability of each class for all recorded time
 276 windows.

277 4.3 Clustering Results

278 The results of the Bayesian Gaussian mixture model analysis are visualized in Fig.
 279 4 for avalanche 3023. They show the predicted classes with a probability higher than 0.3
 280 for each window based on the trained model, together with a Gaussian kernel density
 281 estimation (Scott, 2015) for each class over both space and time. We can observe that
 282 both parts of the avalanche are classified within the same class S2 and that class S1 emerges
 283 30 s before the avalanche propagates over the fiber-optic array. In addition, classes S3
 284 and S4 are also associated with the avalanche, following the time after class S2 emerges.
 285 From the comparison of the kernel densities of the clustering result to the normalized
 286 cumulative GEODAR intensity, we can see a correlation of classes S2 to S4 with the ground
 287 truth of the GEODAR data.

288 5 Discussion: Physical Interpretation of the classes

289 Because the only available ground-truth data with spatial extent in the form of GEO-
 290 DAR data to highlight the physical extent of the avalanches, it is difficult to verify the
 291 hypotheses presented in this chapter. The provided physical interpretation given in this
 292 section should be seen as a highly speculative first attempt to illuminate the DAS avalanche
 293 recordings. Nevertheless, our interpretations are backed up by physical evidence from
 294 the properties of the different classes.

295 Since Bayesian Gaussian mixture models give us a probability distribution of any
 296 feature set being part of one specific class, we can predict the classes of our data to ex-
 297 tract apparent phase velocity ranges, frequency content and dominant propagation di-
 298 rection of the measured signals. The clustering results for all investigated avalanches,
 299 as well as the mean feature values are visualized in Fig. 5. The results show consistency
 300 over all events and we show details of the space-time dependent classification of the DAS
 301 signals for Avalanche 3023 in Fig. 4.

302 Fig. 5 shows that whereas the classes denoted as noise N1 to N6 exhibit consistently
 303 low values in fk amplitudes (features M and S), they can be distinguished from each
 304 other in terms of apparent phase velocities and frequency ranges. Classes N1 and N2 con-
 305 sist of windows with dominant frequencies of ≤ 0.5 Hz. The noise classes N5 and N6 con-
 306 tain mainly frequencies above 5 Hz at apparent phase velocities higher than the ones from
 307 class N1 to N3 (> 350 m/s).

308 Class S3 is associated with the highest overall fk amplitudes at a mean frequency
 309 of around 16 Hz and a mean velocity of 1075 m/s, propagating both uphill and down-
 310 hill along the cable (mean $C \approx 1.05$). This class can be interpreted as the **seismic near-**

Avalanche 3023

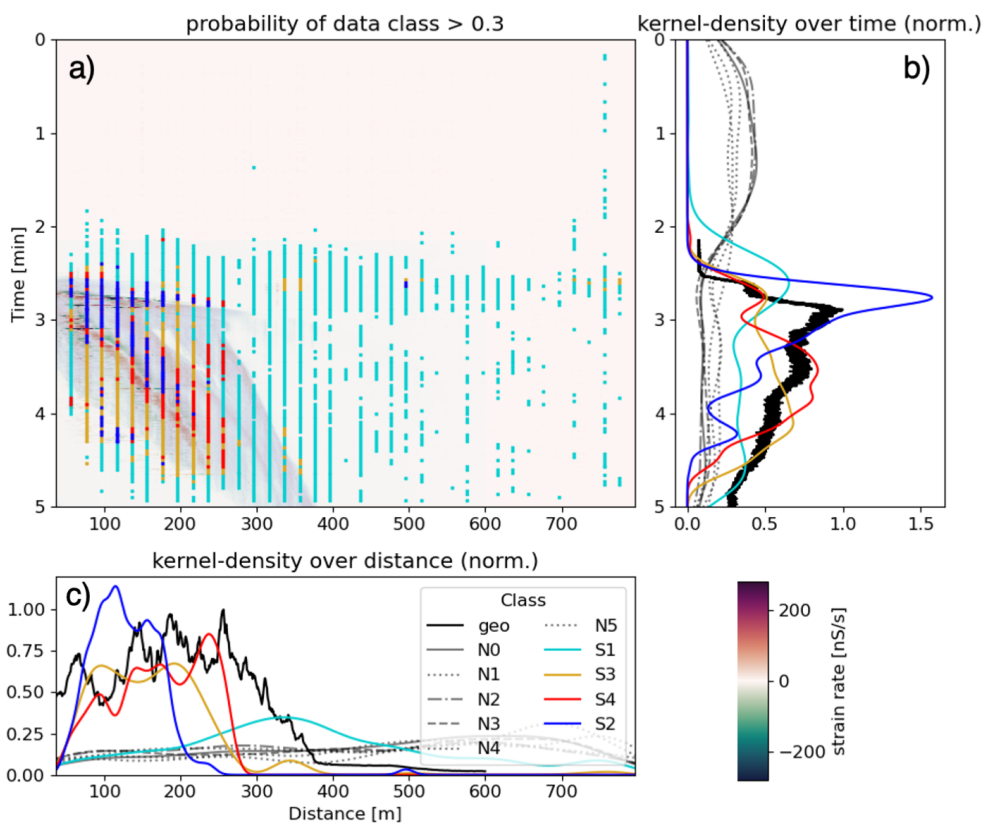


Figure 4. **a)** Results of the predicted classes with a probability above 0.3 for each window of the Bayesian Gaussian mixture model clustering for avalanche 3023. The raw strain-rate data are plotted in the background (see colorbar at the bottom right), whereas the predicted classes are color-coded for each class. The ground truth of the extent of the avalanche is highlighted in transparent blue from the measurements of the GEODAR system. Six different "noise" classes could be identified which are not visualized here (N1 to N6). These classes most likely capture environmental and anthropogenic noise, as well as self-noise of the instrumentation. **b)** Estimated probability density from a Gaussian kernel density over the samples within each class over time. The black line indicates the normalized cumulative GEODAR amplitudes for the given window. **c)** Estimated probability density from a Gaussian kernel over the samples within each class over space. The black line indicates the normalized cumulative GEODAR amplitudes for the given window

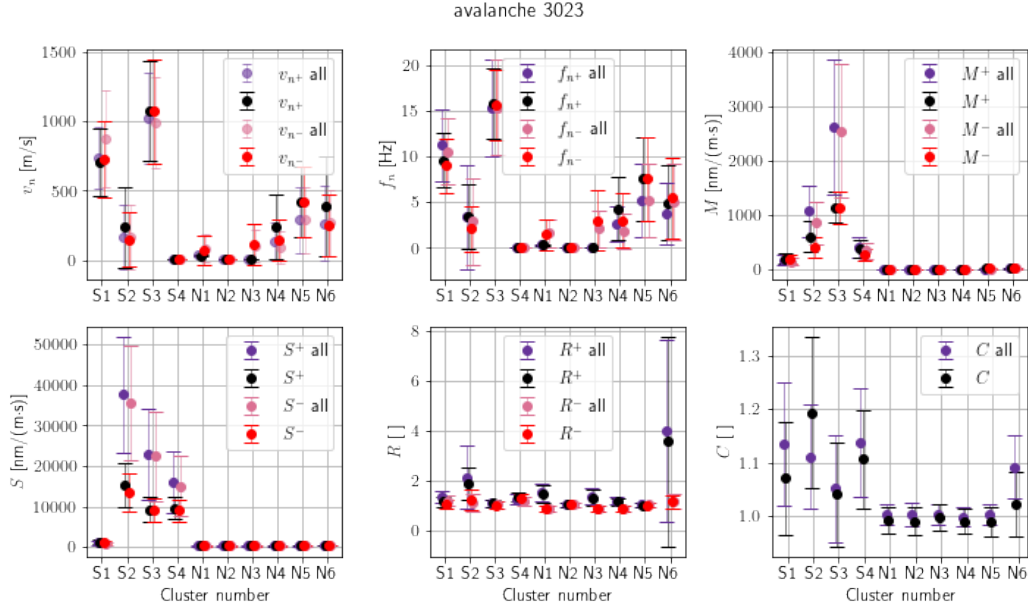


Figure 5. Mean feature values (dots) and $\frac{1}{2}$ standard deviation (error bars) for each clustered feature set of avalanche 3023. Black color indicates positive wavenumber-values (downward propagating energy, superscript $+$) and red indicates negative wavenumbers (upward propagating energy, superscript $-$) along the fiber for avalanche 3023. The purple and light red colors indicate the features for all the training data that were used in the clustering process.

311 **field**, as this class is dominant on channels during the time the avalanche is on top of
 312 the cable. These values are realistic for seismic waves in sediment layers (Boore & Joyner,
 313 1997), especially considering that near-field signals consist of multiple seismic phases in-
 314 cluding P-waves. These are faster than Rayleigh phases, which are the dominant far-field
 315 response to vertical particle-ground impacts (Sánchez-Sesma et al., 2011).

316 Class S2 has a significantly lower mean frequency (3.4 Hz) and apparent velocity
 317 (238 m/s). This class has the highest mean C value (1.2), meaning that the dominant
 318 propagation direction of these signals is downhill. The apparent velocities are exception-
 319 ally low but could be explained by slow Biot’s waves propagating through the pore space
 320 of snow within the avalanche and/or the underlying substrate (Capelli et al., 2016).

321 Based on the apparent velocity content (mean 703 m/s) of class S1, we interpret
 322 it as the **seismo-acoustic far-field** generated by the avalanches. This apparent veloc-
 323 ity is reasonable for surface and S-waves in generic rock sites (Boore & Joyner, 1997).
 324 The frequency content (mean 9.6 Hz) of this class is comparable to the frequency range
 325 of seismic waves generated by avalanches observed in the literature (Van Herwijnen &
 326 Schweizer, 2011). The probability of class S1 increases already 30 s before the avalanche
 327 arrives at the cable. With the above mean frequency, mean velocity and typical avalanche
 328 speeds of several meters per second, this likely corresponds to a time when the avalanche
 329 is several wavelengths away from the cable, which supports our hypothesis of seismic far-
 330 field waves.

331 Class S4 contains frequencies below 1 Hz, which we interpret as quasi-static ground
 332 deformation in response to the instantaneous avalanche weight and frictional shear forces.
 333 Waves of such quasi-static ground deformation can result from flow depth, velocity or
 334 particle concentration perturbations traveling within the avalanche body (Viroulet et al.,

2018) and erosion-deposition mechanisms (Edwards & Gray, 2015). This explains the apparent phase velocities (< 6 m/s), associated with avalanche motion rather than seismic energy propagation of classes S1-S3. The motion of the avalanche front and major secondary surges induce wavelets with periods of ten seconds or longer (Fig. 2b, for example), which are not resolvable with our 5 second time window sizes. Nevertheless, class S4 seems to capture the highest frequencies of these signals. C values of larger than 1.1 indicate that S4 signals propagate preferentially downhill. Uphill propagation, however, is also possible and can be explained by shock wave dispersion (Liu & Mei, 1994).

So far we have discussed the avalanche signal in terms of dominant classes. However, this binary (dominant/non-dominant) characterization is not always justified since several classes may reach similar probabilities at the same location in space and time. This is particularly apparent for Avalanche 3016, whose DAS signals and kernel densities have a simple appearance since the avalanche consists of only one surge (Fig. 6). During times when Avalanche 3016 covers the cable, further signal details are visible and might be interpreted as the avalanche front (1), internal roll waves (2) or erosion-deposition waves (3) and stopping phases (4) (Razis et al., 2014; Viroulet et al., 2018; Tregaskis et al., 2022), travelling at different and variable speeds (different event move-outs in Fig. 6). In addition to class S4, classes S2 and S3 can also be expected to characterize these internal dynamic processes within the avalanche as like class S4 they dominate during times when the avalanche locates above the cable. In fact, for Avalanche 3016, kernel densities of classes S2, S3 and S4 increase and decrease parallel to each other and have comparable peaks (Fig. 6 panel b)).

From this figure we can also observe that the avalanche front propagates at a relatively high apparent group velocity of about 40 m/s (labeled (1)). Internal apparent phase velocities of up to 160 m/s are present in the earlier part of the avalanche (2). We can also observe the transition from class S2 towards S4 (panel b). This may be related to the transition from the erosive and intermittent flow-regime characteristic of the avalanche front towards the depositional flow regime at the avalanche tail (3) after around 3 min. The internal velocities of up to 160 m/s within the avalanche that are higher than the front propagation speed of around 40 m/s suggest that internal phases may be processes related to roll-waves activity taking place at the surface of the denser basal layer (Razis et al., 2014; Viroulet et al., 2018).

The above discussion shows that although different classes can be associated with characteristic ranges of frequencies and propagation velocities, they combine to describe avalanche dynamics. The arrival of the front with its instantaneous increase in local weight will induce low-frequency, quasi-static elastic deformation (class S4). This adds to weight variations resulting from snow entrainment, which for powder snow avalanches can take the form of violent eruptions (Carroll et al., 2012; Sovilla et al., 2006) and other internal phases or flow-depth variations like roll waves (Razis et al., 2014; Viroulet et al., 2018) to produce further low-frequency signals. At the avalanche front, we also expect the turbulent and suspended mass movement to couple into the ground (classes 1 and 3). Although we are not aware of theoretical descriptions of the seismogenesis of turbulent and laminar air-snow mixtures, an equivalent mechanism has been proposed for river flow (Gimbert et al., 2014). This leads to a mixing of signals from classes 1, 3 and 4. Similarly, temperature-dependent sintering produces macroscopic granules (Steinkogler et al., 2015) whose ground impacts generate high-frequency seismic signals (Tsai et al., 2012) constituting classes 1 and 3. It is not clear if these mechanisms also generate the slow seismic phases of class 2, which is a predominant signal when all avalanches override the cable. The existence of a potential Biot phase (Capelli et al., 2016) is possible but not the only explanation. The records of the local M 1.2 earthquake from Sanetschpass about 10 km from our recording site testify to the non-uniqueness of physical class meaning (see event 3036 in the supplementary material, occurring on March 03, 2021, 00:38:14 UTC): The DAS earthquake records lack class S4, which is expected as the earthquake

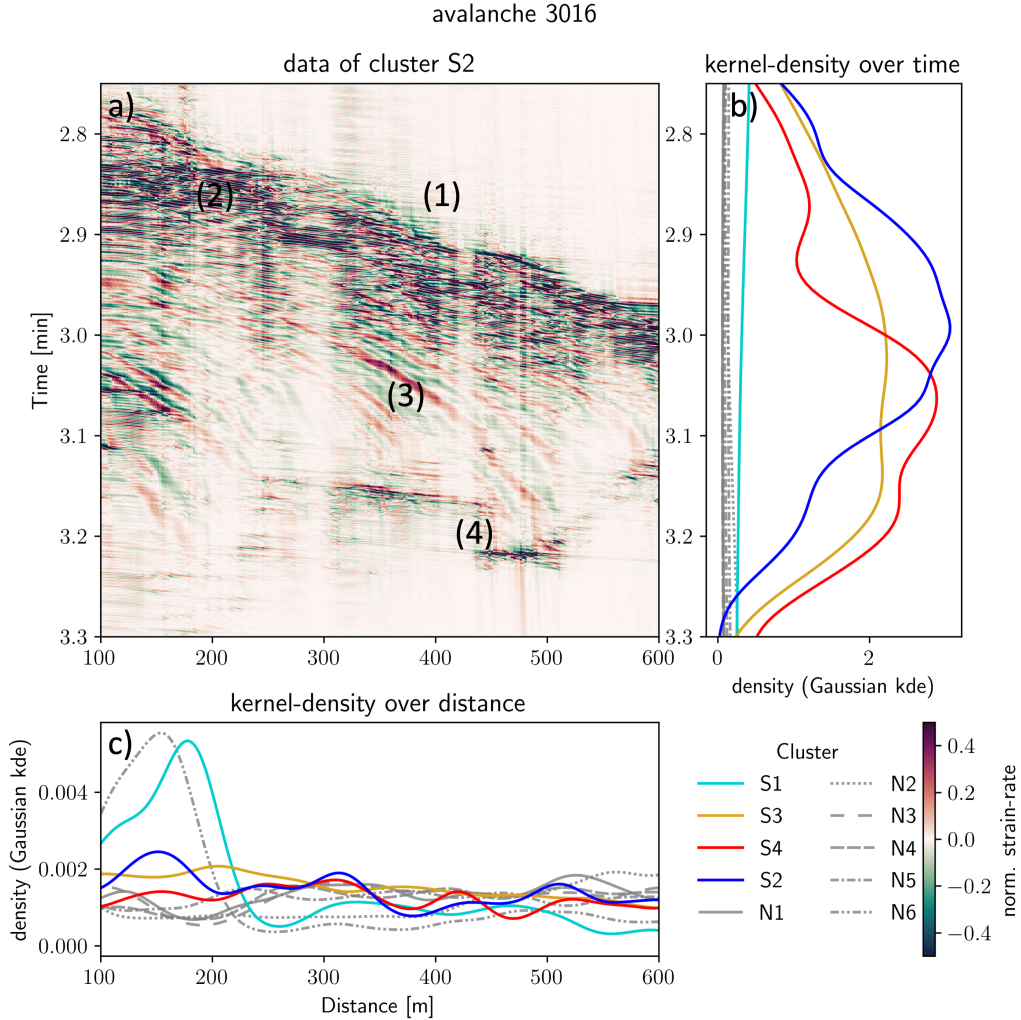


Figure 6. **a)** DAS data of avalanche 3016 in the frequency range from 0.001 to 5 Hz for apparent velocities between 1 and 250 m/s (corresponding to the mass-movement class S2). We can observe that the internal structure of the avalanche is more complex than for avalanche 3023. The group velocity of the avalanche front (1) is approximately 40 m/s, whereas the phase velocity inside the avalanche (2) is around 160 m/s. The later part of the avalanche lacks these high-velocity arrivals, and instead consists of events that decrease from 40 m/s until they stop (3). In the deposit area, other events (4) also seem to propagate at apparent phase velocities of > 160 m/s downhill. **b)** Estimated probability density from a Gaussian kernel density over the samples within each class over time. **c)** Estimated probability density from a Gaussian kernel over the samples within each class over space.

388 does not generate slowly propagating signals corresponding to the quasi-static elastic ground
 389 deformation induced by an avalanche. On the other hand, the earthquake records are
 390 predominantly classified into classes S1 and S3. Our interpretation of S3 as near-field
 391 seismic signals at frequencies resolvable within 5 second time windows is questionable
 392 since the earthquake located 10 km away from the cable. The absence of class S2 sug-
 393 gests that this class is indeed characteristic for mass movements, even though an expla-
 394 nation of its rather slow seismic propagation speeds remains elusive.

395 To summarize, there exist distinct signal classes, which are shared among all of the
 396 recorded avalanches (classes S1 to S4). Class S1 is interpreted as the seismo-acoustic far-
 397 field that arrives at the cable before the mass movement itself. Classes S2-S4 are asso-
 398 ciated with low-frequency, quasi-static ground deformation, near-field ground shaking
 399 and other yet-to-be-confirmed signals generated as the avalanches override the cable. Al-
 400 though these interpretations may differ for other seismic sources like earthquakes, the
 401 signal classification seems to be characteristic for all of our avalanches and could be used
 402 for automatic detection.

403 5.1 Internal avalanche characteristics

404 We identified that class S2 is most likely related to the physical properties of the
 405 mass-movement inside the avalanche. We can use this to further analyse the internal struc-
 406 ture of the avalanche propagating over the fiber-optic array. Since avalanche 3023 does
 407 not have a complex internal avalanche structure, but a well separated slow and fast part,
 408 we will look at a different avalanche. We chose avalanche 3016 for this analysis, since it
 409 is a single surge avalanche with a complex internal structure. From the clustering anal-
 410 ysis, we know the frequency and apparent phase-velocity ranges of the mass-movement
 411 class S2. Hence, we focus on frequencies < 5 Hz and apparent phase velocities < 250
 412 m/s (only downward propagating). The DAS data of a zoomed-in version of avalanche
 413 3016 within this frequency and velocity range are displayed in Fig. 6.

414 Accordingly, we explain the low apparent phase velocities (< 6 m/s) with the avalanche's
 415 bulk mass motion, which may vary between avalanche events or even between surges of
 416 a single avalanche (Figure 2). Hence, in terms of avalanche processes, the classes S2 and
 417 S4 could be associated to different flow regimes within the avalanche - where the ear-
 418 lier class S2 may correspond to the high-energy processes occurring at the front of the
 419 avalanche, such as entrainment of snow or impacts of the (turbulent) suspensions with
 420 the ground, and class S4 may be related to the signal generated by the following dense
 421 basal layer and its deposition (Köhler, McElwaine, & Sovilla, 2018).

422 Another observation is, that the presence of some mass movement classes by them-
 423 selves require additional analysis. A regional M 1.5 earthquake from Sanetschpass (see
 424 event 3036 in the supplementary material) is predominantly classified into classes S1 and
 425 S3. The classification of S1 and S3 during the regional earthquake also indicate that ad-
 426 ditional signals might be included in these classes. The absence of class S2 indicates that
 427 there is no mass movement present during the earthquake, but this non-uniqueness of
 428 the classification needs to be kept in mind for potential automatic classifications in the
 429 future.

430 6 Perspectives for Snow Avalanche Monitoring

431 DAS enables the distributed measurement of ground deformation in response to
 432 avalanche flow with high temporal and spatial resolution. There exist specific reasons
 433 why this could be a game changer for avalanche monitoring and warning applications.
 434 Our analysis shows that non-supervised classification of DAS recordings containing both
 435 noise and avalanche signatures is capable of separating the two. Although this method
 436 has to be applied to longer (multiple months) DAS records to evaluate its accuracy, the
 437 signal classes shared among all recorded avalanches suggests that automatic detections
 438 are feasible. The consistent detections of class S1 signals tens of seconds prior to the avalanche
 439 arrivals at the cable are particularly encouraging: interrogating pre-installed communi-
 440 cation cables seems to be sensitive enough to detect avalanche seismograms remotely.
 441 This is important for the more realistic case where fiber-optic infrastructure locates par-
 442 allel to pass roads or train lines, which are threatened by avalanche hazards in the lat-
 443 eral slopes and couloirs. For such cases snow avalanches will cross rather than propa-
 444 gate along fiber optic cables and longitudinal wave propagation as presented here will

445 be reduced. We can nevertheless expect to measure the seismic phases of classes S1, S2
 446 and S3, which could be used to distinguish between powder snow avalanches contain-
 447 ing a turbulent flow and pure dense snow avalanches (Köhler, Fischer, et al., 2018). How
 448 exactly such flow regime distinction manifests itself in the recognition of class S1, S2 and
 449 S3 signals remains to be seen. It may be necessary to further support classification with
 450 transition probabilities between states as has been done in previous application of ma-
 451 chine learning algorithms to avalanche seismograms (Hammer et al., 2017; Heck et al.,
 452 2018). Finally, we stress the advantage of our Gaussian mixture models allowing for dif-
 453 ferent states to coexist at the same time rather than identifying one single dominant state.
 454 Future classification could thus be improved with relative probabilities so that the "state
 455 mix" describes different parts and kinds of avalanches.

456 Our processing leverages signal coherence over a set of spatially distributed seis-
 457 mic sensors. Equivalent signal processing has already been used in the past for seismic
 458 signals of avalanches in the form of array methods (Lacroix & Helmstetter, 2011; Heck,
 459 Van Herwijnen, et al., 2019). In the present case, the unprecedented amount of seismic
 460 sensing locations was combined with unsupervised machine learning to automatically clas-
 461 sify signals. To this, future applications could add waveform features (Chmiel et al., 2021)
 462 and image processing to further improve classification accuracy (Thrustarson et al., 2021).
 463 In any case, we do not expect user-defined threshold rules to perform better than our
 464 machine learning scheme since such methods cannot distinguish between signals with sim-
 465 ilar seismic amplitudes and frequency content.

466 Whereas this study focused on snow avalanches, the proposed DAS observation and
 467 signal classification could also be applied to other granular media like debris flows, rock-
 468 ice avalanches and smaller slope failures. Given seismogenesis of water turbulence (Gimbert
 469 et al., 2014), flood waves could be monitored and detected, as well. Our signals show that
 470 DAS is able to detect internal avalanche processes, which could be manifestations of roll-
 471 waves or shock waves. These internal waves are general features of open surface flows
 472 (Liu & Mei, 1994). Shock waves propagate as flow depth perturbations with larger waves
 473 traveling faster, which allows them to grow by "swallowing" smaller waves. The succes-
 474 sive merging explains pulsing behavior of granular flows and frontal flow depths, which
 475 are much larger and thus more destructive than expected for steady flow (Zanuttigh &
 476 Lamberti, 2007; Razis et al., 2014; Viroulet et al., 2018). The detection of internal waves,
 477 which our DAS measurements provide, could therefore be a tool for better understand-
 478 ing and predicting maximum flow depths of granular flows and floods.

479 7 Challenges

480 Since the apparent phase velocity of an event propagating along the fiber is strongly
 481 dependent on the incidence angle of the event, it needs to be treated as a site- and event-
 482 specific property. Hence, the transferability of the trained Gaussian mixture model from
 483 the given test site to other installations might be limited. Nevertheless, the physical in-
 484 tuition we gained from the analyzed avalanches can be transferred to other sites and ca-
 485 ble layouts.

486 A big challenge for monitoring hazardous alpine mass movements with DAS is the
 487 existence and access to fiber-optic infrastructure. Whereas the Vallée de la Sionne test
 488 site had accessible infrastructure existing for decades, sites like this are rare. The dis-
 489 tribution of existing fibers in rural alpine areas, especially those that are subject to fre-
 490 quent hazardous mass movements, can be limited. In addition to fiber access, stable long-
 491 term power access for the interrogation unit can be challenging. If no fiber-optic infras-
 492 tructure for data transfer exists, real-time monitoring and immediate early warning re-
 493 quire a stable data transfer from the interrogation unit to the local responsible author-
 494 ities. In case the fiber-optic infrastructure is required to be installed, the fiber needs to
 495 be protected against mass movement induced damages. For avalanche monitoring this
 496 means that the cable needs to be trenched deep enough and be protected against ero-

497 sion processes. We believe that the DAS technology can not only improve our understand-
498 ing of hazardous mass movements from a scientific point of view by highlighting inter-
499 actions between the mass movement and the subsurface, but can also improve seismic
500 hazard monitoring and early warning solutions in the near-future.

501 **8 Conclusions and Outlook**

502 We have shown that the DAS technology is capable to measure avalanches prop-
503 agating towards and on top of a fiber-optic cable. The avalanche signals measured from
504 such a system include the seismo-acoustic near- and far-field as well as various mass move-
505 ment regimes. By combining DAS with Bayesian Gaussian mixture models, we are able
506 to extract key avalanche characteristics and their developments over both space and time.
507 Significant importance for the classification are both the frequency content and the ap-
508 parent phase velocities of the data within local time-space windows.

509 DAS adds new observations to the toolbox of mass movement research. With high-
510 resolution recordings, DAS delivers data from the interface of the avalanche with the (sub)surface
511 of the Earth. We observed indications of roll-waves. In the future, it can be envisioned
512 that the Froude number could be calculated from the apparent velocities if the depth
513 of the flow is known (similar to Pérez- Guillén et al. (2016)). Further research in am-
514 plitude calibration of DAS systems for mass movements is required, but a site-specific
515 flow regime characterization based on DAS recordings and physical properties of strain
516 rate measurements can be envisioned in the future.

517 The incorporation of subsurface strain (rate) as observed with DAS into numer-
518 ical avalanche simulation tools could increase the usability of DAS data in the field of
519 avalanche dynamics research even further.

520 **Acknowledgments**

521 The authors want to thank everyone involved in the field campaign and the discussion
522 of the results. Especially, we want to thank Emma Suriñach for constructive discussions
523 about seismic measurements of avalanches. Our colleagues at WSL, SLF and ETH Zürich
524 for feedback on the data processing and the applied methods, and Athena Chalari and
525 the Silixa support team for their technical assistance of our iDAS(TM) interrogation unit.
526 PP also wants to acknowledge the IRIS DAS research coordination network, especially
527 discussions within their Machine Learning working group.

528 **Data availability statement**

529 The data of the two avalanche examples will be made available upon publication
530 on Zenodo in the Snow Avalanche Dynamics Community. Since the Bayesian Gaussian
531 Mixture model depends on a wide range of tuning parameters, the trained model will
532 be made available. The extracted features for both avalanche examples will also be made
533 available upon publication.

534 **Appendix A Schematic Avalanche Propagating Over DAS Array**

535 **Appendix B Background Information on Avalanches Discussed in this** 536 **Manuscript**

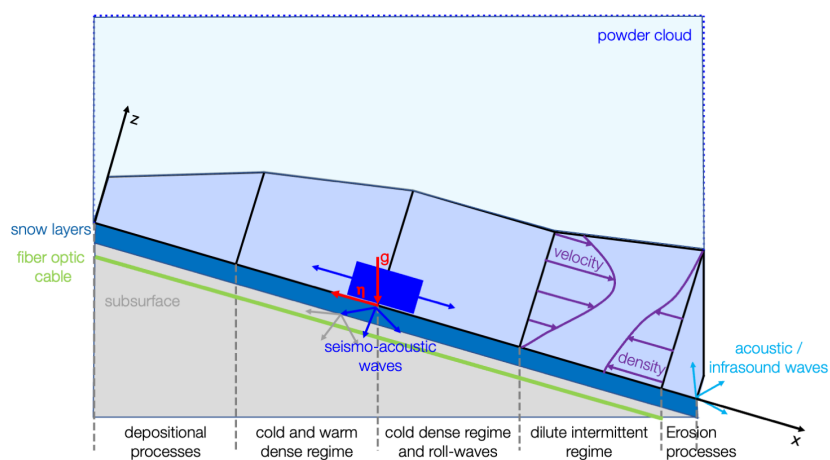


Figure A1. Schematic avalanche processes generating seismo-acoustic signals. The velocity and density profile vary with depth (z). The propagation of the avalanche downhill (x) results in acoustic infrasound waves in the air, as well as seismo-acoustic waves due to sliding friction, depositional mechanisms, and interaction of the mass movement with the topography. In this experiment, the fiber-optic cable is located in a conduit in the subsurface, over which the avalanches propagate. Figure schematically after Pérez-Guillén et al. (2016) and Sovilla et al. (2015).

Table B1. Avalanche characteristics of the events discussed in this manuscript. The duration indicates the time the avalanches are propagating on top of the fiber-optic array.

Number	Date of occurrence	Duration	Characteristics
Avalanche 3005	2021-01-02	? minutes	- Very small avalanche - Did not reach the cable - No surges visible
Avalanche 3009	2021-01-15	4 minutes	- Large transitional powder snow avalanche - Fast and dilute component - 3 main surges - Depositional tail
Avalanche 3016	2021-01-25	1 minute	- Powder snow avalanche - No dense transition - Depositional tail
Avalanche 3020	2021-01-27	0.5 minutes	- Small powder snow avalanche - No dense transition - One surge
Avalanche 3021	2021-01-28	1 minute	- Dense avalanche - Depositional tail - One big surge
Avalanche 3022	2021-01-28	2.5 minutes	- Large transitional powder snow avalanche - Depositional tail
Avalanche 3023	2021-01-28	3 minutes	- Large powder snow avalanche - Partial transition - Fast and slow part - Well separated - Long tail
Avalanche 3024	2021-01-28	? minutes	- Large transitional powder snow avalanche - Not over array
Avalanche 3026	2021-01-31	? minutes	- No avalanche visible
Avalanche 3027	2021-02-01	? minutes	- Small one-surge powder snow avalanche - Not over array
Avalanche 3028	2021-02-01	? minutes	- Large multi-surge snow avalanche - Not over array - Too far away
Avalanche 3030	2021-02-08	? minutes	- No avalanche visible
Event 3036	2021-03-03	< 0.3 minutes	- Regional earthquake M1.2 at Sanetschpass - No avalanche

Appendix C Additional plots

Additional plots of the avalanche candidates in Tab. B1 with their corresponding predicted classes from the clustering algorithm can be found in the supplementary material.

References

- Allstadt, K. E., Matoza, R. S., Lockhart, A. B., Moran, S. C., Caplan-Auerbach, J., Haney, M. M., ... Malone, S. D. (2018). Seismic and acoustic signatures of surficial mass movements at volcanoes. *Journal of Volcanology and Geothermal Research*, *364*, 76-106. Retrieved from <https://www.sciencedirect.com/science/article/pii/S0377027317306261> doi: <https://doi.org/10.1016/j.jvolgeores.2018.09.007>
- Alpaydin, E. (2020). *Introduction to machine learning*. MIT press.
- Ammann, W. J. (1999). A new swiss test-site for avalanche experiments in the vallée de la sionne/valais. *Cold Regions Science and Technology*, *30*(1-3), 3-11.
- Arattano, M., & Marchi, L. (2008). Systems and sensors for debris-flow monitoring and warning. *Sensors*, *8*(4), 2436-2452.
- Bishop, C. M., & Nasrabadi, N. M. (2006). *Pattern recognition and machine learning* (Vol. 4) (No. 4). Springer.
- Boore, D. M., & Joyner, W. B. (1997). Site amplifications for generic rock sites. *Bulletin of the seismological society of America*, *87*(2), 327-341.
- Capelli, A., Kapil, J. C., Reiweger, I., Or, D., & Schweizer, J. (2016). Speed and attenuation of acoustic waves in snow: Laboratory experiments and modeling with biot's theory. *Cold Regions Science and Technology*, *125*, 1-11.
- Carroll, C., Turnbull, B., & Louge, M. (2012). Role of fluid density in shaping eruption currents driven by frontal particle blow-out. *Physics of Fluids*, *24*(6), 066603.
- Chmiel, M., Walter, F., Wenner, M., Zhang, Z., McArdell, B. W., & Hibert, C. (2021). Machine learning improves debris flow warning. *Geophysical Research Letters*, *48*(3), e2020GL090874. Retrieved from <https://agupubs.onlinelibrary.wiley.com/doi/abs/10.1029/2020GL090874> (e2020GL090874 2020GL090874) doi: <https://doi.org/10.1029/2020GL090874>
- Dilley, M. (2005). *Natural disaster hotspots: a global risk analysis* (Vol. 5). World Bank Publications.
- Edwards, A., & Gray, J. (2015). Erosion-deposition waves in shallow granular free-surface flows. *Journal of Fluid Mechanics*, *762*, 35-67.
- Emberson, R., Kirschbaum, D., & Stanley, T. (2020). New global characterisation of landslide exposure. *Natural Hazards and Earth System Sciences*, *20*(12), 3413-3424.
- Froude, M. J., & Petley, D. N. (2018). Global fatal landslide occurrence from 2004 to 2016. *Natural Hazards and Earth System Sciences*, *18*(8), 2161-2181.
- Gimbert, F., Tsai, V. C., & Lamb, M. P. (2014). A physical model for seismic noise generation by turbulent flow in rivers. *Journal of Geophysical Research: Earth Surface*, *119*(10), 2209-2238.
- Grimm, J. (2021). Cryoseismic event analysis on distributed strain recordings leveraging statistical learning methods. *MSc. Thesis, ETH Zürich*.
- Grimm, J., & Poli, P. (2022). *Making sense of urban data with clustering of coherence-based array features* (Tech. Rep.). EGU2022: Copernicus Meetings.
- Hammer, C., Fäh, D., & Ohrnberger, M. (2017). Automatic detection of wet-snow avalanche seismic signals. *Natural hazards*, *86*(2), 601-618.
- Hartog, A. H. (2017). *An introduction to distributed optical fibre sensors*. CRC press.
- Heck, M., Hammer, C., van Herwijnen, A., Schweizer, J., & Fäh, D. (2018). Au-

- 589 tomatic detection of snow avalanches in continuous seismic data using hidden
590 markov models. *Natural Hazards and Earth System Sciences*, 18(1), 383–396.
- 591 Heck, M., Hobiger, M., Van Herwijnen, A., Schweizer, J., & Fäh, D. (2019). Local-
592 ization of seismic events produced by avalanches using multiple signal classifi-
593 cation. *Geophysical Journal International*, 216(1), 201–217.
- 594 Heck, M., Van Herwijnen, A., Hammer, C., Hobiger, M., Schweizer, J., & Fäh, D.
595 (2019). Automatic detection of avalanches combining array classification and
596 localization. *Earth Surface Dynamics*, 7(2), 491–503.
- 597 Iten, M., Puzrin, A. M., & Schmid, A. (2008). Landslide monitoring using a road-
598 embedded optical fiber sensor. In W. Ecke, K. J. Peters, & N. G. Meyendorf
599 (Eds.), *Smart sensor phenomena, technology, networks, and systems 2008* (Vol.
600 6933, pp. 328 – 336). SPIE. Retrieved from [https://doi.org/10.1117/](https://doi.org/10.1117/12.774515)
601 12.774515 doi: 10.1117/12.774515
- 602 Keylock, C., Ash, M., Vriend, N., Brennan, P., McEwaine, J., & Sovilla, B. (2014).
603 Looking inside an avalanche using a novel radar system. *Geology Today*, 30(1),
604 21–25.
- 605 Klaasen, S., Paitz, P., Lindner, N., Dettmer, J., & Fichtner, A. (2021). Dis-
606 tributed acoustic sensing in volcano-glacial environments—mount meager,
607 british columbia. *Journal of Geophysical Research: Solid Earth*, 126(11),
608 e2021JB022358. Retrieved from [https://agupubs.onlinelibrary.wiley](https://agupubs.onlinelibrary.wiley.com/doi/abs/10.1029/2021JB022358)
609 .com/doi/abs/10.1029/2021JB022358 (e2021JB022358 2021JB022358) doi:
610 <https://doi.org/10.1029/2021JB022358>
- 611 Köhler, A., Fischer, J.-T., Scandroglio, R., Bavay, M., McElwaine, J., & Sovilla,
612 B. (2018). Cold-to-warm flow regime transition in snow avalanches. *The*
613 *Cryosphere*, 12(12), 3759–3774.
- 614 Köhler, A., McElwaine, J., & Sovilla, B. (2018). Geodar data and the flow regimes
615 of snow avalanches. *Journal of geophysical research: earth surface*, 123(6),
616 1272–1294.
- 617 Lacroix, P., & Helmstetter, A. (2011). Location of seismic signals associated with
618 microearthquakes and rockfalls on the séchilienne landslide, french alps. *Bul-*
619 *letin of the Seismological Society of America*, 101(1), 341–353.
- 620 Leinss, S., Wicki, R., Hostenstein, S., Baffelli, S., & Bühler, Y. (2020). Snow
621 avalanche detection and mapping in multitemporal and multiorbital radar
622 images from terrasar-x and sentinel-1. *Natural Hazards and Earth System*
623 *Sciences*, 20(6), 1783–1803.
- 624 Lindsey, N. J., Dawe, T. C., & Ajo-Franklin, J. B. (2019). Illuminating seafloor
625 faults and ocean dynamics with dark fiber distributed acoustic sensing. *Sci-*
626 *ence*, 366(6469), 1103–1107.
- 627 Lindsey, N. J., & Martin, E. R. (2021). Fiber-optic seismology. *Annual Review of*
628 *Earth and Planetary Sciences*, 49, 309–336.
- 629 Lindsey, N. J., Rademacher, H., & Ajo-Franklin, J. B. (2020). On the broadband
630 instrument response of fiber-optic das arrays. *Journal of Geophysical Research:*
631 *Solid Earth*, 125(2), e2019JB018145.
- 632 Liu, K.-f., & Mei, C. C. (1994). Roll waves on a layer of a muddy fluid flowing down
633 a gentle slope—a bingham model. *Physics of Fluids*, 6(8), 2577–2590.
- 634 Marchetti, E., Walter, F., Barfucci, G., Genco, R., Wenner, M., Ripepe, M., . . .
635 Price, C. (2019). Infrasound array analysis of debris flow activity and im-
636 plication for early warning. *Journal of Geophysical Research: Earth Sur-*
637 *face*, 124(2), 567–587. Retrieved from [https://agupubs.onlinelibrary](https://agupubs.onlinelibrary.wiley.com/doi/abs/10.1029/2018JF004785)
638 .wiley.com/doi/abs/10.1029/2018JF004785 doi: [https://doi.org/10.1029/](https://doi.org/10.1029/2018JF004785)
639 2018JF004785
- 640 Marchetti, E., Walter, F., & Meier, L. (2021). Broadband infrasound sig-
641 nal of a collapsing hanging glacier. *Geophysical Research Letters*, 48(16),
642 e2021GL093579.
- 643 Martin, E. R., Huot, F., Ma, Y., Cieplicki, R., Cole, S., Karrenbach, M., & Biondi,

- 644 B. L. (2018). A seismic shift in scalable acquisition demands new processing:
 645 Fiber-optic seismic signal retrieval in urban areas with unsupervised learning
 646 for coherent noise removal. *IEEE Signal Processing Magazine*, *35*(2), 31–40.
- 647 Michlmayr, G., Chalari, A., Clarke, A., & Or, D. (2017). Fiber-optic high-resolution
 648 acoustic emission (ae) monitoring of slope failure. *Landslides*, *14*(3), 1139–
 649 1146.
- 650 Minardo, A., Catalano, E., Coscetta, A., Zeni, G., Zhang, L., Di Maio, C., ...
 651 Zeni, L. (2018). Distributed fiber optic sensors for the monitoring of
 652 a tunnel crossing a landslide. *Remote Sensing*, *10*(8). Retrieved from
 653 <https://www.mdpi.com/2072-4292/10/8/1291> doi: 10.3390/rs10081291
- 654 Paitz, P., Edme, P., Gräff, D., Walter, F., Doetsch, J., Chalari, A., ... Fichtner, A.
 655 (2021). Empirical investigations of the instrument response for distributed
 656 acoustic sensing (das) across 17 octaves. *Bulletin of the Seismological Society
 657 of America*, *111*(1), 1–10.
- 658 Pedregosa, F., Varoquaux, G., Gramfort, A., Michel, V., Thirion, B., Grisel, O., ...
 659 Duchesnay, E. (2011). Scikit-learn: Machine learning in Python. *Journal of
 660 Machine Learning Research*, *12*, 2825–2830.
- 661 Petley, D. (2012). Global patterns of loss of life from landslides. *Geology*, *40*(10),
 662 927–930.
- 663 Press, W. H., Teukolsky, S. A., Vetterling, W. T., & Flannery, B. P. (2007). *Numerical
 664 recipes 3rd edition: The art of scientific computing*. Cambridge university
 665 press.
- 666 Prokop, A., Schön, P., Wirbel, A., & Jungmayr, M. (2014). Monitoring avalanche
 667 activity using distributed acoustic fiber optic sensing. In *Proceedings of the in-
 668 ternational snow science workshop* (pp. 129–133).
- 669 Pérez- Guillén, C., Sovilla, B., Suriñach, E., Tapia, M., & Köhler, A. (2016). De-
 670 ducing avalanche size and flow regimes from seismic measurements. *Cold
 671 Regions Science and Technology*, *121*, 25-41. Retrieved from [https://
 672 www.sciencedirect.com/science/article/pii/S0165232X15002177](https://www.sciencedirect.com/science/article/pii/S0165232X15002177) doi:
 673 <https://doi.org/10.1016/j.coldregions.2015.10.004>
- 674 Razis, D., Edwards, A., Gray, J., & van der Weele, K. (2014). Arrested coarsening of
 675 granular roll waves. *Physics of Fluids*, *26*(12), 123305.
- 676 Sánchez-Sesma, F. J., Weaver, R. L., Kawase, H., Matsushima, S., Luzón, F., &
 677 Campillo, M. (2011). Energy partitions among elastic waves for dynamic
 678 surface loads in a semi-infinite solid. *Bulletin of the Seismological Society of
 679 America*, *101*(4), 1704–1709.
- 680 Scott, D. W. (2015). *Multivariate density estimation: theory, practice, and visualiza-
 681 tion*. John Wiley & Sons.
- 682 Sovilla, B., Burlando, P., & Bartelt, P. (2006). Field experiments and numerical
 683 modeling of mass entrainment in snow avalanches. *Journal of Geophysical Re-
 684 search: Earth Surface*, *111*(F3).
- 685 Sovilla, B., McElwaine, J. N., & Louge, M. Y. (2015). The structure of powder
 686 snow avalanches. *Comptes Rendus Physique*, *16*(1), 97-104. Re-
 687 trieved from [https://www.sciencedirect.com/science/article/pii/
 688 S1631070514001844](https://www.sciencedirect.com/science/article/pii/S1631070514001844) (Granular physics / Physique des milieux granulaires)
 689 doi: <https://doi.org/10.1016/j.crhy.2014.11.005>
- 690 Steinkogler, W., Gaume, J., Löwe, H., Sovilla, B., & Lehning, M. (2015). Granula-
 691 tion of snow: From tumbler experiments to discrete element simulations. *Jour-
 692 nal of Geophysical Research: Earth Surface*, *120*(6), 1107–1126.
- 693 SwissTopo. (2021). *Online tool for Swiss Raster images*. [https://www.swisstopo
 694 .admin.ch/de/geodata/maps/smr/smr10.html](https://www.swisstopo.admin.ch/de/geodata/maps/smr/smr10.html). ([Online; accessed 24-
 695 February-2022])
- 696 Thrastarson, S., Torfason, R., Klaasen, S., Paitz, P., CUBUK SABUNCU, Y.,
 697 Jónsdóttir, K., & Fichtner, A. (2021). Detecting seismic events with computer
 698 vision: Applications for fiber-optic sensing. *Earth and Space Science Open*

- 699 *Archive*, 19. Retrieved from <https://doi.org/10.1002/essoar.10509693.1>
700 doi: 10.1002/essoar.10509693.1
- 701 Tregaskis, C., Johnson, C., Cui, X., & Gray, J. (2022). Subcritical and supercritical
702 granular flow around an obstacle on a rough inclined plane. *Journal of Fluid*
703 *Mechanics*, 933.
- 704 Tsai, V. C., Minchew, B., Lamb, M. P., & Ampuero, J.-P. (2012). A physical model
705 for seismic noise generation from sediment transport in rivers. *Geophysical Re-*
706 *search Letters*, 39(2).
- 707 Van Herwijnen, A., & Schweizer, J. (2011). Monitoring avalanche activity using a
708 seismic sensor. *Cold Regions Science and Technology*, 69(2-3), 165–176.
- 709 Viroulet, S., Baker, J. L., Rocha, F. M., Johnson, C. G., Kokelaar, B. P., & Gray,
710 J. M. N. T. (2018). The kinematics of bidisperse granular roll waves. *Journal*
711 *of Fluid Mechanics*, 848, 836–875. doi: 10.1017/jfm.2018.348
- 712 Walter, F., Gräff, D., Lindner, F., Paitz, P., Köpfl, M., Chmiel, M., & Fichtner,
713 A. (2020). Distributed acoustic sensing of microseismic sources and wave
714 propagation in glaciated terrain. *Nature communications*, 11(1), 1–10.
- 715 Wenner, M., Allstadt, K., Thelen, W., Lockhart, A., Hirschberg, J., Mc Ardell,
716 B. W., & Walter, F. (2022). Seismometer records of ground tilt induced
717 by debris flows. *Bulletin of the Seismological Society of America*, 112(5),
718 2376–2395.
- 719 Williams, E. F., Fernández-Ruiz, M. R., Magalhaes, R., Vanthillo, R., Zhan, Z.,
720 González-Herráez, M., & Martins, H. F. (2019). Distributed sensing of mi-
721 croseisms and teleseisms with submarine dark fibers. *Nature communications*,
722 10(1), 1–11.
- 723 Yu, Z., Dai, H., Zhang, Q., Zhang, M., Liu, L., Zhang, J., & Jin, X. (2018).
724 High-resolution distributed strain sensing system for landslide monitoring.
725 *Optik*, 158, 91-96. Retrieved from [https://www.sciencedirect.com/](https://www.sciencedirect.com/science/article/pii/S0030402617316418)
726 [science/article/pii/S0030402617316418](https://www.sciencedirect.com/science/article/pii/S0030402617316418) doi: [https://doi.org/10.1016/](https://doi.org/10.1016/j.ijleo.2017.12.013)
727 [j.ijleo.2017.12.013](https://doi.org/10.1016/j.ijleo.2017.12.013)
- 728 Zanuttigh, B., & Lamberti, A. (2007). Instability and surge development in debris
729 flows. *Reviews of Geophysics*, 45(3).
- 730 Zhan, Z. (2019). Distributed Acoustic Sensing Turns Fiber-Optic Cables into Sensi-
731 tive Seismic Antennas. *Seismological Research Letters*, 91(1), 1-15. Retrieved
732 from <https://doi.org/10.1785/0220190112> doi: 10.1785/0220190112
- 733 Zhongming, Z., Linong, L., Xiaona, Y., Wangqiang, Z., & Wei, L. e. a. (2021). Ar6
734 climate change 2021: The physical science basis. *2021 IPCC report*.